FREE VIBRATION OF AXIALLY LOADED FUNCTIONALLY GARED CARBON NANOTUBE-REINFORCED COMPOSITE CURVED BEAMS

Nguyen Ngoc Hieu[a], Phan Thanh Thi[a], Bui Van Tai[a], Nguyen Ngoc Duong[a,*]

[a]Faculty of Civil Engineering, Ho Chi Minh City University of Technology and Education, No. 1 Vo Van Ngan Street, Thu Duc Ward, Ho Chi Minh City, Vietnam

Abstract

This study analyzes the free vibration of axially graded functionally graded carbon nanotube-reinforced composite (FG-CNTRC) curved beams. The theoretical framework employed is based on higher-order shear deformation theory. The governing equations are formulated using the Lagrange equation. A Ritz procedure is implemented to compute the beams' natural frequencies and critical buckling loads under diverse boundary conditions. Several numerical examples are presented to substantiate the efficacy of the proposed theory and method. Furthermore, the study explores the influences of boundary condition, curvature, slenderness ratio, distribution pattern, and fractional volume of the reinforcing materials on the free vibration and buckling behaviors of the FG-CNTRC curved beams.

Keywords: FG-CNTRC curved beam; higher-order shear deformation theory; Ritz method; free vibration; buckling.

1. Introduction

Carbon nanotubes (CNTs) have been recognized as a highly effective reinforcement material for polymer composites owing to their exceptional elastic modulus, tensile strength, and low density. The potential applications of polymer/CNT composites extend to enhancing structural integrity and developing high-performance multifunctional composites. Functionally graded (FG) materials also exhibit a gradual variation in one or more properties throughout their volume. This enables functionally graded carbon nanotube-reinforced composites (FG-CNTRC) to possess tailored characteristics customized to meet specific performance requirements [1–3]. Furthermore, curved beams are integral to various natural and engineering applications [4]. The challenging conditions in which these curved beams operate necessitate their ability to withstand extreme circumstances, including mechanical loads, temperature fluctuations, and exposure to various environmental factors. Any minor inaccuracies in predicting the behavior of these structures could lead to significant implications for both human safety and the integrity of property [4]. Consequently, a growing number of researchers have proposed various methodologies to capture these beams' response behaviors. Among these, free vibration and buckling responses are critical factors that require in-depth exploration [5, 6].

Several theories have examined the behavior of FG-CNTRC arch beams. The Euler-Bernoulli theory is the most straightforward approach; however, neglecting shear deformations renders this theory unsuitable for analyzing deep beams. Consequently, first-order shear deformation theory (FSDT) has been utilized to study the mechanical responses of FG-CNTRC curved beams. For instance,

---

Corresponding author. E-mail address: duongnn@hcmute.edu.vn (Duong, N. N.)

Shi et al. [7] applied FSDT along with a semi-analytical solution to investigate the behavior of FG-CNTRC curved beams, while Allahkarami et al. [8] focused on the buckling response of FG-CNTRC curved microbeams. Although FSDT accounts for shear deformations, it requires a shear correction coefficient, the accurate determination of which can be challenging in general cases. Therefore, higher-order shear deformation theories (HSDTs) have been proposed. For examples, Zhang et al. [9] explored the nonlinear bending response of FG-CNTR arches resting on a foundation using Reddy's shear deformation theory and a two-step perturbation technique. Babaei [10] investigated the nonlinear free vibration and instability of FG CNTRC arch nanobeams utilizing HSDT, two-step perturbation techniques, and the Galerkin method. Lezgy-Nazargah et al. [11] analyzed the vibration, buckling, and bending responses of FG sandwich curved beams using a global-local refined shear deformation theory. It is seen that the accuracy and efficacy of HSDT are dependent on the shear function [4]. Recently, Phung et al. [12] proposed a shear function based Chebyshev polynomial and applied for analysis of functionally graded triply periodic minimal surface plates. Furthermore, quasi-3D theories have been employed to investigate FG-CNTRC curved beams to account for the effects of normal deformations [6].

In terms of methodology, various approaches have been developed for the analysis of curved beams, including the Navier method, differential transform method, dynamic stiffness matrix method, transfer matrix method, and finite element method, among others [4, 13–15]. Sayyad and Ghugal [16] analyzed the static behavior of functionally graded sandwich curved beams utilizing the Navier solution. Hong [17] introduced a novel isogeometric analysis model incorporating a modified first-order shear theory for analyzing the buckling, free vibration, and transient response of double-layer bidirectional functionally graded porous curved beams on a foundation. Recently, the Ritz method has been further developed to investigate composite curved beams by Nguyen et al. [18].

Based on the literature review, research on FG-CNTRC curved beams remains relatively scarce. Theoretically, very few studies have utilized the HSDT. Moreover, the Ritz method has not been widely employed in analyzing FG-CNTRC curved beams. To the author, no studies have yet examined the free vibration of axially loaded FG-CNTRC beams using HSDT and the Ritz method. Therefore, this study aims to develop the Ritz solution in conjunction with HSDT to analyze the free vibration of axially loaded FG-CNTRC curved beams. The governing equations will be established based on Lagrange's equation. Numerical examples will be performed to validate the proposed method and to investigate the influence of boundary condition, curvature, types of carbon nanotube distribution, and volume fraction on the beams' critical loads and natural frequencies.

2. Theory and formulations

2.1. FG-CNTRC curved beams

An FG-CNTRC curved beam, composed of a combination of carbon nanotubes and an isotropic polymer matrix, is examined in this study. The dimensions of the curved beam are defined by its length (L), thickness (h), width (b), and radius of curvature (R), as depicted in Fig. 1(a). This research considers four distinct reinforcement patterns across the cross sections of the curved beams, as illustrated in Fig. 1(b). The effective material properties of the FG-CNTRC curved beams can be determined using the rule of mixtures. Consequently, the formulations for the effective Young's modulus and shear modulus of the FG-CNTRC beams are presented as follows [5, 6, 19]:

$$E_{11} = \eta_1 V_{CNT} E_{11}^{CNT} + V_m E_m \tag{1}$$

$$\frac{\eta_2}{E_{22}} = \frac{V_{CNT}}{E_{22}^{CNT}} + \frac{V_m}{E_m} \tag{2}$$

$$\frac{\eta_3}{G_{12}} = \frac{V_{CNT}}{G_{12}^{CNT}} + \frac{V_m}{G_m} \tag{3}$$

where $E_{11}^{CNT}, E_{22}^{CNT}$, and G_{12}^{CNT} represent Young's modulus and shear modulus of the CNTs, respectively. E_m and G_m denote the corresponding material properties of the polymer matrix. Additionally, V_{CNT} and V_m are the volume fractions of the carbon nanotubes and the polymer matrix, respectively, satisfying the relationship $V_{CNT} + V_m = 1$. The parameters η_1, η_2, and η_3 define the efficiency coefficients of the CNTs. Furthermore, the Poisson's ratio (v) and mass density (ρ) of the FG-CNTRC curved beams are expressed as follows [5]:

$$v = V_{CNT}v_{CNT} + V_m v_m \tag{4}$$

$$\rho = V_{CNT}\rho_{CNT} + V_m \rho_m \tag{5}$$

where v_{CNT} and v_m represent the Poisson's ratios, ρ_{CNT} and ρ_m denote the densities of the CNTs and the polymer matrix, respectively. For the various patterns of carbon nanotube reinforcement distributed across the cross sections of the beams, as illustrated in Fig. 1(b), the continuous mathematical functions utilized to characterize the distributions of the material constituents are provided as follows [5, 6, 20]:

UC: $$V_{CNT}(z) = V_{CNT}^* \tag{6}$$

VC: $$V_{CNT}(z) = V_{CNT}^* \left(1 + \frac{2z}{h}\right) \tag{7}$$

OC: $$V_{CNT}(z) = V_{CNT}^* \left(2 - \frac{4|z|}{h}\right) \tag{8}$$

XC: $$V_{CNT}(z) = V_{CNT}^* \frac{4|z|}{h} \tag{9}$$

where V_{CNT}^* represents the specified volume fraction of CNTs, which can be determined using the following equation [20]:

$$V_{CNT}^* = \frac{w_{CNT}}{w_{CNT} + (\rho_{CNT}/\rho_m)(1 - w_{CNT})} \tag{10}$$

where w_{CNT} denotes the mass fraction of CNTs. In this investigation, the CNTs of efficiency parameters (η_i) corresponding to the specified volume fraction V_{CNT}^* are as follows: $\eta_1 = 1.2833$ and $\eta_2 = \eta_3 = 1.0556$ for the case of $V_{CNT}^* = 0.12$; $\eta_1 = 1.3414$ and $\eta_2 = \eta_3 = 1.7101$ for the case of $V_{CNT}^* = 0.17$; $\eta_1 = 1.3238$ and $\eta_2 = \eta_3 = 1.7380$ for the case of $V_{CNT}^* = 0.28$ [5, 20].

2.2. Higher-order shear deformation theory

The displacement field based a higher-order shear deformation theory, which comprises the *x*-direction (u_1) and the *z*-direction (u_3), can be expressed Eqs. (11) and (12). It can be observed that the present theory based on quasi-3D theory while neglecting the higher-order terms associated with thickness stretching components [6, 21]:

$$u_1(x, z, t) = (1 + \frac{z}{R})u_0(x, t) - zw_{0,x}(x, t) + T(z)\left[w_{0,x}(x, t) + \theta_0(x, t) - \frac{u_0(x, t)}{R}\right] \tag{11}$$

$$u_3(x, z, t) = w_0(x, t) \tag{12}$$
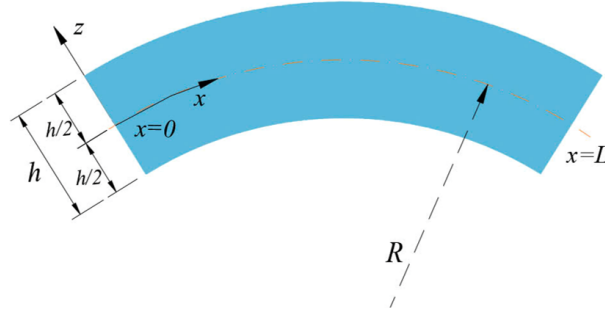
(a) Geometry of FG-CNTRC curved beam

UC　　　　XC　　　　OC　　　　VC
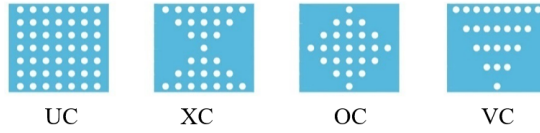
(b) Four typical distribution patterns

Figure 1. Geometry of FG-CNTRC curved beam

where the displacements of a point on the mid-surface in the x- and z-directions are denoted by u_0 and w_0, respectively. Furthermore, θ_0 represents the rotation of the transverse normal about the y-axis, while $T(z) = \cos\left[3\cos^{-1}\left(\dfrac{z}{h}\right)\right]$ denotes the shear function proposed by Phung et al. [12].

The strain field is articulated as follows:

$$\varepsilon_{xx} = \frac{\partial u_1}{\partial x} + \frac{w_0}{R} = \left(1 + \frac{z}{R}\right)u_{0,x} - zw_{0,xx} + T\left(w_{0,xx} + \theta_{0,x} - \frac{u_{0,x}}{R}\right) + \frac{w_0}{R} \tag{13}$$

$$\gamma_{xz} = \frac{\partial u_1}{\partial z} + \frac{\partial u_3}{\partial x} - \frac{u_0}{R} = T_{,z}\left(w_{0,x} + \theta_0 - \frac{u_0}{R}\right) \tag{14}$$

The strain and stress relations are presented as:

$$\sigma_{xx} = Q_{11}\varepsilon_{xx} = \left[E_{11}/\left(1 - v^2\right)\right]\varepsilon_{xx}; \quad \sigma_{xz} = Q_{55}\gamma_{xz} = G_{12}\gamma_{xz} \tag{15}$$

2.3. Variational formulation

The total energy (Π) of the FG-CNTRC curved beam is presented as follows [6, 10, 16]:

$$\Pi = \Pi_E + \Pi_V - \Pi_K \tag{16}$$

where Π_E, Π_K, and Π_V represent the strain energy, kinetic energy, and the work done by the axial force (N_0) of the beam, which are detailed in Eqs. (17), (20), and (22) as follows [6, 16]:

$$\begin{aligned}
\Pi_E &= \frac{1}{2}\int_V \left(\sigma_{xx}\varepsilon_{xx} + \sigma_{xz}\gamma_{xz}\right)dV \\
&= \frac{1}{2}\int_0^L
\begin{bmatrix}
\left(A + \dfrac{2B}{R} + \dfrac{C}{R^2} - \dfrac{2D}{R} - \dfrac{2E}{R^2} + \dfrac{F}{R^2}\right)u_{0,x}^2 + \dfrac{G}{R^2}u_0^2 + 2\left(D + \dfrac{E}{R} - \dfrac{F}{R}\right)u_{0,x}\theta_{0,x} \\[2mm]
-\dfrac{2G}{R}u_0\theta_0 + 2\left(-\dfrac{C}{R} + D - B - \dfrac{F}{R} + \dfrac{2E}{R}\right)u_{0,x}w_{0,xx} - \dfrac{2G}{R}u_0w_{0,x} + 2G\theta_0w_{0,x} \\[2mm]
+ 2\left(\dfrac{A}{R} + \dfrac{B}{R^2} - \dfrac{F}{R^2}\right)u_{0,x}w_0 + G\theta_0^2 + F\theta_{0,x}^2 + 2\left(-E + F\right)\theta_{0,x}w_{0,xx} \\[2mm]
+ \dfrac{2D}{R}\theta_{0,x}w_0 + \dfrac{A}{R^2}w_0^2 + (C + F - 2E)w_{0,xx}^2 + Gw_{0,x}^2 + 2\left(\dfrac{D}{R} - \dfrac{B}{R}\right)w_0w_{0,xx}
\end{bmatrix}dx
\end{aligned} \tag{17}$$

where

$$(A, B, C, D, E, F) = \int_{-h/2}^{h/2} Q_{11} \left(1, z, z^2, T, Tz, T^2\right) bdz \tag{18}$$

$$G = \int_{-h/2}^{h/2} Q_{55} T_{,z}^2 bdz \tag{19}$$

$$\Pi_K = \frac{1}{2} \int_V \rho \left[\left(\frac{\partial u_1}{\partial t}\right)^2 + \left(\frac{\partial u_3}{\partial t}\right)^2\right] dV$$

$$= \frac{1}{2} \int_0^L \left[\begin{array}{l} \left(H + \dfrac{2I}{R} + \dfrac{J}{R^2} - \dfrac{2K}{R} - \dfrac{2M}{R^2} + \dfrac{N}{R^2}\right)\left(\dfrac{\partial u_0}{\partial t}\right)^2 + 2\left(K + \dfrac{M}{R} - \dfrac{N}{R}\right)\dfrac{\partial u_0}{\partial t}\dfrac{\partial \theta_0}{\partial t} \\[3mm] + 2\left(-I - \dfrac{J}{R} + K + \dfrac{2M}{R} - \dfrac{N}{R}\right)\dfrac{\partial u_0}{\partial t}\dfrac{\partial w_{0,x}}{\partial t} + N\left(\dfrac{\partial \theta_0}{\partial t}\right)^2 + 2\left(-M + N\right)\dfrac{\partial \theta_0}{\partial t}\dfrac{\partial w_{0,x}}{\partial t} \\[3mm] + H\left(\dfrac{\partial w_0}{\partial t}\right)^2 + (J - 2M + N)\left(\dfrac{\partial w_{0,x}}{\partial t}\right)^2 \end{array} \right] dx \tag{20}$$

where

$$(H, I, J, K, M, N) = \int_{-h/2}^{h/2} \rho \left(1, z, z^2, T, zT, T^2\right) bdz \tag{21}$$

$$\Pi_V = -\frac{1}{2} \int_0^L N_0 \left(w_{0,x} - \frac{u_0}{R}\right)^2 dx = -\frac{1}{2} \int_0^L N_0 \left(w_{0,x}^2 - \frac{2}{R}u_0 w_{0,x} + \frac{u_0^2}{R^2}\right) dx \tag{22}$$

It is stated that this study is based on the assumption of small deformations and disregards geometric non-linearity. Therefore, the work performed by the axial force considers the influence of the beam's curvature as presented in Eq. (22). This formula has also been employed by Huynh et al. [22] and Karamanli et al. [21] in the analysis of FG curved beams.

2.4. Solution

The Ritz method is utilized to approximate the displacement field as follows [18, 23]:

$$u_0(x, t) = \sum_{j=1}^{m} u_{0j}\psi_j e^{i\omega t}; \quad w_0(x, t) = \sum_{j=1}^{m} w_{0j}\varphi_j e^{i\omega t}; \quad \theta_0(x, t) = \sum_{j=1}^{m} \theta_{0j}\xi_j e^{i\omega t} \tag{23}$$

where ω is natural frequency; $i^2 = -1$; u_{0j}, w_{0j} and θ_{0j} are unknown parameters; $\psi_j(x), \varphi_j(x)$ and $\xi_j(x)$ are shape functions as indicated in Table 1 [18]. In this study, six typical boundary conditions (BC), including Hinged-Simply supported (HS), Hinged-Hinged (HH), Clamped-Free (CF), Clamped-Simply supported (CS), Clamped-Hinged (CH), and Clamped-Clamped (CC), are investigated. Their essential boundary conditions are presented as follows:

HS: $u_0(0) = w_0(0) = w_0(L) = 0$ (24)

HH: $u_0(0) = w_0(0) = u_0(L) = w_0(L) = 0$ (25)

CF: $u_0(0) = w_0(0) = w_{0,x}(0) = \theta_0(0) = 0$ (26)

CS: $u_0(0) = w_0(0) = w_{0,x}(0) = \theta_0(0) = w_0(L) = 0$ (27)

CH: $u_0(0) = w_0(0) = w_{0,x}(0) = \theta_0(0) = u_0(L) = w_0(L) = 0$ (28)

CC: $u_0(0) = w_0(0) = w_{0,x}(0) = \theta_0(0) = u_0(L) = w_0(L) = w_{0,x}(L) = \theta_0(L) = 0$ (29)

Table 1. The shape functions for various boundary conditions [18]

BC	s	r	**P**	**Q**	$\varphi_j(x)$	$\psi_j(x)$	$\xi_j(x)$
HS	1	0	1	0	$\zeta_j(x)$	$\varpi_j(x)$	$\zeta_{j,x}(x)$
HH	1	1	1	1	$\zeta_j(x)$	$\varpi_j(x)$	$\zeta_{j,x}(x)$
CF	1	0	0	0	$\zeta_j(x)$	$\varpi_j(x)$	$\varpi_j(x)$
CS	2	1	(0,1)	0	$\zeta_j(x)$	$\varpi_j(x)$	$\varpi_j(x)$
CH	2	1	(0,1)	1	$\zeta_j(x)$	$\varpi_j(x)$	$\varpi_j(x)$
CC	3	1	(0,1,1)	1	$\zeta_j(x)$	$\varpi_j(x)$	$\varpi_j(x)$

As indicated in Table 1, the shape functions $\psi_j(x), \varphi_j(x)$, and $\xi_j(x)$ are represented by the basis-functions $\zeta_j(x)$ and $\varpi_j(x)$ as follows [18]:

$$\zeta_j(x) = \prod_{k=1}^{j}\left(\frac{F_k - 1}{F_j} - \frac{x}{L}\right) \times \prod_{k=1}^{s}\left(\mathbf{P}_k - \frac{x}{L}\right) \tag{30}$$

$$\varpi_j(x) = \prod_{k=1}^{j}\left(\frac{F_k - 1}{F_j} - \frac{x}{L}\right) \times \prod_{k=1}^{r}\left(\mathbf{Q}_k - \frac{x}{L}\right) \tag{31}$$

where F_k is Fibonacci sequence. For specific boundary conditions, the parameters $r, s, \mathbf{P}$, and $\mathbf{Q}$ are selected to meet the essential boundary conditions (Eqs. (24)–(29)) as shown in Table 1.

Substituting Eq. (23) into Eq. (22) and applying the Lagrange's equation as described below:

$$\frac{\partial \Pi}{\partial u_{0j}} - \frac{d}{dt}\frac{\partial \Pi}{\partial(\partial u_{0j}/\partial t)} = 0; \quad \frac{\partial \Pi}{\partial w_{0j}} - \frac{d}{dt}\frac{\partial \Pi}{\partial(\partial w_{0j}/\partial t)} = 0; \quad \frac{\partial \Pi}{\partial \theta_{0j}} - \frac{d}{dt}\frac{\partial \Pi}{\partial(\partial \theta_{0j}/\partial t)} = 0 \tag{32}$$

This process will yield the governing equation of the free vibration for axially loaded FG-CNTRC curved beams as follows:

$$\left(\mathbf{K} - N_0\mathbf{K_G} - \omega^2\mathbf{M}\right)\mathbf{d} = \mathbf{0} \tag{33}$$

where $\mathbf{d}$ represents the column vector of unknown parameters, and $\mathbf{K}, \mathbf{M}$, and $\mathbf{K_G}$ denote the stiffness, mass, and geometric matrices, respectively. The components of $\mathbf{K}, \mathbf{M}$, and $\mathbf{K_G}$ are articulated in Appendix [6].

3. Numerical examples

In this section, numerical examples are conducted to validate the method and theory. Additionally, these results are employed to assess the influence of boundary condition, slenderness, curvature, distribution pattern and fractional volume of reinforced materials on the free vibration and buckling behaviors of FG-CNTRG curved beams. The material properties are assumed as follows: for CNT material $E_{11}^{CNT} = 600$ GPa, $E_{22}^{CNT} = 10$ GPa, $G_{12}^{CNT} = 17.2$ GPa, $v_{12}^{CNT} = 0.19$, $\rho_{CNT} = 1400$ kg/m^3; For polymer matrix $E_m = 2.5$ GPa, $v_m = 0.3$, $\rho_m = 1190$ kg/m^3. For simplification, the dimensionless formulas are utilized [6]:

$$\text{Dimensionless fundamental frequency (DFF): } \bar{\omega} = \omega L^2/h\sqrt{\rho_m/E_m} \tag{34}$$

$$\text{Dimensionless critical buckling load (DCBL): } \bar{N}_{cr} = N_{cr}L^2/bh^3 E_m \tag{35}$$

3.1. Convergence study

To investigate the convergence of the method, FG-CNTRC curved beams ($V_{CNT}^* = 0.12$, $L/h = 5$, $R/L = 15$, UC) under various boundary conditions are considered. Table 2 presents the DFF and DCBL of the beam with respect to m. It is observed that the method converges when $m = 8$ across all boundary conditions. Consequently, this value will be employed in the numerical examples throughout the remainder of the paper.

Table 2. Convergence study for DFF and DCBL of FG-CNTRC curved beams
($L/h = 5$, $R/L = 15$, $V_{CNT}^* = 0.12$, UC)

BC	m								
	2	3	4	5	6	7	8	9	10
DFF									
HS	8.914	8.603	8.603	8.602	8.602	8.602	8.602	8.602	8.602
HH	9.091	8.820	8.820	8.819	8.819	8.819	8.819	8.819	8.819
CF	4.231	4.099	4.071	4.055	4.053	4.052	4.051	4.051	4.051
CS	11.255	9.753	9.628	9.588	9.574	9.570	9.569	9.569	9.569
CH	11.375	9.927	9.810	9.774	9.760	9.756	9.755	9.755	9.755
CC	11.216	11.207	11.037	11.037	11.022	11.022	11.022	11.022	11.022
DCBL									
HS	8.144	7.690	7.690	7.688	7.688	7.688	7.688	7.688	7.688
HH	8.453	8.066	8.066	8.064	8.064	8.064	8.064	8.064	8.064
CF	4.542	4.511	4.511	4.511	4.511	4.511	4.511	4.511	4.511
CS	9.344	8.697	8.684	8.682	8.682	8.682	8.682	8.682	8.682
CH	9.534	8.990	8.973	8.970	8.970	8.970	8.970	8.970	8.970
CC	10.715	10.685	10.537	10.537	10.535	10.535	10.535	10.535	10.535

3.2. Parametric study

The DFF and DCBL of FG-CNTRC curved beams with various boundary conditions (HS, HH, CF, CS, CH, and CC), slenderness ratios ($L/h = 5$ and 20), curvature ratios ($R/L = 5$ and 10), distribution patterns (UC, XC, OC, and VC), and volume fractions (0.12, 0.17, and 0.28) are presented in Tables 3–6. The current results are compared with those reported by Pham et al. [6] utilizing quasi-3D and finite element method. It is seen that there are no significant differences between the present findings and those of Ref. [6]. This observation underscores the effectiveness and accuracy of this study's theoretical framework and theory.

Table 3. DFF of FG-CNTRC curved beams ($L/h = 5$, $R/L = 5$)

V_{CNT}^*	BC	UC		XC		OC		VC	
		Present	Ref. [6]	Present	Ref. [6]	Present	Ref. [6]	Present	Ref. [6]
0.12	HS	8.5241	-	8.9386	-	7.4203	-	8.0352	-
	HH	10.3226	10.3522	10.6724	10.7182	9.4008	9.3872	10.9342	10.9690
	CF	4.0544	4.0759	4.3817	4.4133	3.3442	3.3438	3.7255	3.7413
	CS	9.4989	-	9.9134	-	8.3157	-	9.1772	-
	CH	11.0677	11.1667	11.4259	11.5498	10.0610	10.0776	11.3885	11.4810
	CC	12.1433	12.3331	12.5234	12.7508	10.9672	11.0248	11.9767	12.1533

V_{CNT}^*	BC	UC		XC		OC		VC	
		Present	Ref. [6]	Present	Ref. [6]	Present	Ref. [6]	Present	Ref. [6]
0.17	HS	10.8689	-	11.3612	-	9.4546	-	10.1670	-
	HH	12.9443	12.9765	13.3650	13.4100	11.7406	11.7257	13.7962	13.8323
	CF	5.0981	5.1213	5.5100	5.5424	4.1836	4.1830	4.6432	4.6593
	CS	12.1333	-	12.5848	-	10.7046	-	11.6832	-
	CH	13.9411	14.0558	14.3350	14.4724	12.7017	12.7205	14.3645	14.4683
	CC	15.3524	15.5726	15.7389	15.9962	13.9586	14.0248	15.1151	15.3164
0.28	HS	12.0765	-	12.3041	-	10.9920	-	11.5007	-
	HH	14.9264	14.9914	15.1043	15.1667	14.0193	14.0315	15.7670	15.8377
	CF	5.8282	5.8716	6.1348	6.1813	4.9720	4.9847	5.3995	5.4298
	CS	13.4547	-	13.7037	-	12.2864	-	13.1003	-
	CH	15.9410	16.1147	16.1378	16.3182	14.9616	15.0298	16.4306	16.5897
	CC	17.4311	17.7502	17.6547	17.9979	16.2692	16.4102	17.2807	17.5706

Table 4. DFF of FG-CNTRC curved beams ($L/h = 20, R/L = 10$)

V_{CNT}^*	BC	UC		XC		OC		VC	
		Present	Ref. [6]	Present	Ref. [6]	Present	Ref. [6]	Present	Ref. [6]
0.12	HS	16.3273	-	19.0777	-	12.1930	-	13.8594	-
	HH	19.9568	19.9586	22.2672	22.7261	16.7136	16.7066	22.7525	22.7544
	CF	6.1428	6.1426	7.3172	7.3188	4.4947	4.4920	5.1537	5.1530
	CS	22.3945	-	25.1985	-	17.4940	-	19.6819	-
	CH	25.0299	25.0315	27.5868	27.6090	20.7052	20.6729	24.8163	24.8168
	CC	30.6401	30.6762	33.2233	33.3051	25.5875	25.5321	28.0338	28.0560
0.17	HS	19.9282	-	23.3560	-	14.7752	-	16.7940	-
	HH	24.2541	24.2555	27.1428	27.1479	20.1927	20.1856	27.6795	27.6803
	CF	7.4486	7.4480	8.8913	8.8916	5.4193	5.4163	6.2131	6.2118
	CS	27.7139	-	31.2790	-	21.4643	-	24.1385	-
	CH	30.8060	30.8029	34.0714	34.0793	25.2586	25.224	30.3490	30.3448
	CC	38.1353	38.1668	41.4459	41.5118	31.5720	31.5098	34.5802	34.5952
0.28	HS	24.2592	-	27.9382	-	18.2596	-	20.5806	-
	HH	29.8143	29.8267	32.8684	32.8740	25.1140	25.1128	33.9300	33.9411
	CF	9.2009	9.2032	10.8703	10.8717	6.7387	6.7371	7.6902	7.6907
	CS	32.7427	-	36.0108	-	26.1244	-	28.9102	-
	CH	36.8495	36.8839	39.8012	39.8259	31.0120	30.9948	36.7162	36.7338
	CC	44.5508	44.6645	47.1380	47.2466	38.2052	38.1880	41.0481	41.1130

Table 5. DCBL of FG-CNTRC curved beams ($L/h = 5, R/L = 5$)

V_{CNT}^*	BC	UC		XC		OC		VC	
		Present	Ref. [6]	Present	Ref. [6]	Present	Ref. [6]	Present	Ref. [6]
0.12	HS	7.6900	-	8.4488	-	5.8437	-	6.9694	-

V_{CNT}^*	BC	UC		XC		OC		VC	
		Present	Ref. [6]	Present	Ref. [6]	Present	Ref. [6]	Present	Ref. [6]
	HH	10.3064	10.6370	11.0577	11.4828	8.1519	8.2009	9.9637	10.2671
	CF	4.5108	4.5159	5.4926	5.5098	2.9011	2.8888	3.6223	3.6249
	CS	8.6943	-	9.4026	-	6.8180	-	8.1767	-
	CH	10.6863	10.9510	11.4436	11.7571	8.4390	8.5173	10.6753	11.0417
	CC	12.0775	12.4711	12.8934	13.3655	9.0056	9.2171	11.7408	12.1035
0.17	HS	12.6166	-	13.7708	-	9.5792	-	11.2928	-
	HH	17.0779	17.5531	18.0259	18.6187	13.8442	13.9048	16.4518	16.8776
	CF	7.0759	7.0817	8.6591	8.6734	4.4726	4.4574	5.5770	5.5788
	CS	14.3715	-	15.3528	-	11.4254	-	13.4268	-
	CH	17.4715	17.8060	18.4583	18.8590	14.1797	14.2553	17.5395	18.0388
	CC	19.6838	20.2463	20.7154	21.3749	15.2320	15.5234	19.0688	19.5749
0.28	HS	15.8551	-	16.4462	-	13.1745	-	14.6364	-
	HH	21.1348	21.9909	21.6863	22.6332	18.2293	18.5143	20.7206	21.4858
	CF	9.7382	9.7738	11.2467	11.2690	6.6263	6.6243	7.9270	7.9437
	CS	17.8318	-	18.3192	-	15.2970	-	17.0349	-
	CH	22.1878	22.9565	22.8016	23.5633	18.8989	19.2585	22.3274	23.2601
	CC	25.2686	26.2798	25.9686	27.0289	20.1212	20.7891	24.8515	25.7638

Table 6. DCBL of FG-CNTRC curved beams ($L/h = 20, R/L = 10$)

| V_{CNT}^*	BC	UC		XC		OC		VC	
		Present	Ref. [6]	Present	Ref. [6]	Present	Ref. [6]	Present	Ref. [6]
0.12	HS	27.7610	-	37.8941	-	15.4858	-	20.1467	-
	HH	41.2684	41.2754	51.3690	51.4098	28.9435	28.9181	52.4007	52.4164
	CF	8.0318	8.0318	11.6013	11.6043	4.2256	4.2229	5.5855	5.5842
	CS	46.4429	-	59.6465	-	27.8344	-	35.4798	-
	CH	56.2286	56.2681	69.5919	69.7275	37.2666	37.1848	54.4840	54.5099
	CC	79.9310	80.0741	95.5833	95.9401	54.0957	53.9191	65.7431	65.8207
0.17	HS	41.7170	-	57.2915	-	22.9369	-	29.8452	-
	HH	61.4904	61.4969	76.9976	77.0259	42.6204	42.5889	78.3536	78.3644
	CF	11.8433	11.8428	17.1581	17.1596	6.1696	6.1659	8.1526	8.1500
	CS	71.3545	-	92.2505	-	42.0291	-	53.5658	-
	CH	85.6967	85.7438	106.7965	106.9127	55.8853	55.7873	82.2112	82.2272
	CC	124.7109	124.8886	149.9472	150.2964	82.9527	82.7345	100.7379	100.8117
0.28	HS	62.9750	-	83.5043	-	35.6883	-	45.6442	-
	HH	94.6322	94.7112	114.9852	115.0249	67.1503	67.1429	119.2877	119.4007
	CF	18.6519	18.6575	26.6746	26.6763	9.7703	9.7687	12.8338	12.8340
	CS	102.6402	-	126.1823	-	63.8686	-	78.9971	-
	CH	125.5136	125.7857	149.3592	149.5308	85.8728	85.8572	122.3463	122.5221
	CC	173.6946	174.4267	197.4730	198.0525	123.8886	123.9102	144.8119	145.1833

(a) DFF

(b) DCBL
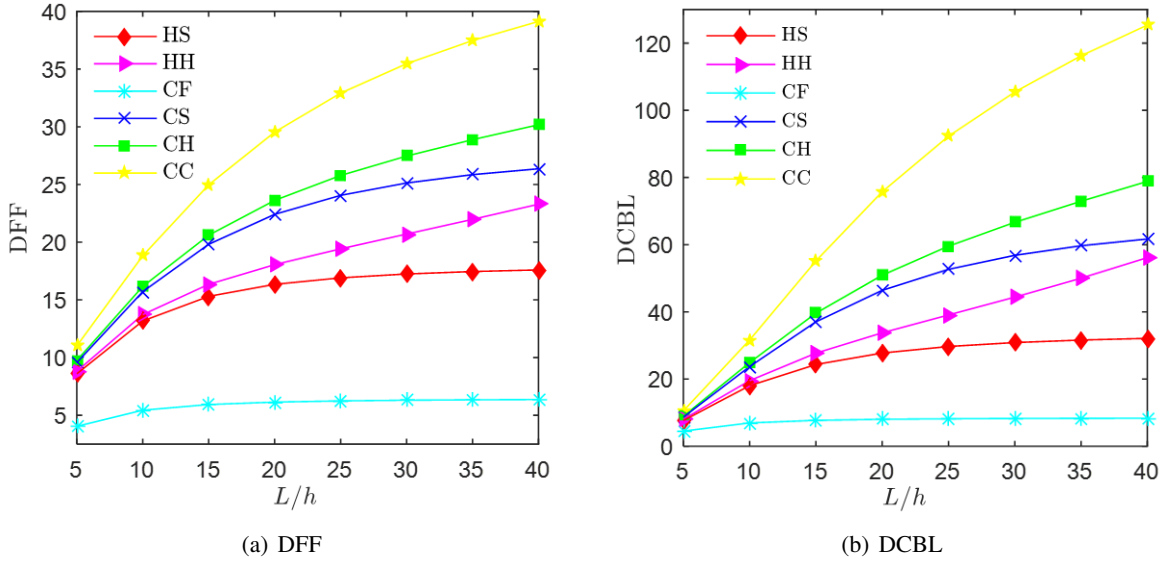
Figure 2. DFF and DCBL of FG-CNTRC curved beams under various BCs with respect to L/h
($R/L = 15$, $V^*_{CNT} = 0.12$, UC)
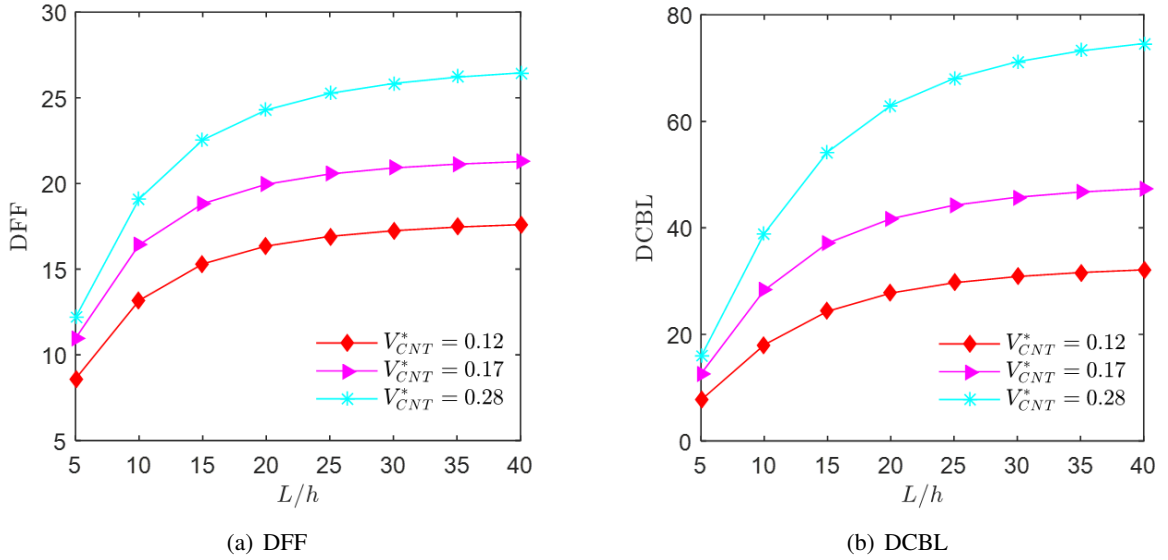

(a) DFF

(b) DCBL

Figure 3. DFF and DCBL of FG-CNTRC curved beams under various volume fractions with respect to L/h
($R/L = 15$, HS, UC)

Figs. 2(a) and 2(b) illustrate the variation of the DFF and DCBL of the beam ($R/L = 15$, $V^*_{CNT} = 0.12$, UC) under different boundary conditions as a function of the L/h ratio. It can be observed that as the L/h ratio increases, both DFF and DCBL also rise across all boundary conditions. This trend corroborates findings by Pham et al. [6]. Furthermore, the DFF and DCBL are maximized for the CC beam and minimized for the CF beam. This indicates that the constraints at both ends of the beam significantly influence its overall stiffness; specifically, the overall stiffness is highest for the CC BC and lowest for the CF one.
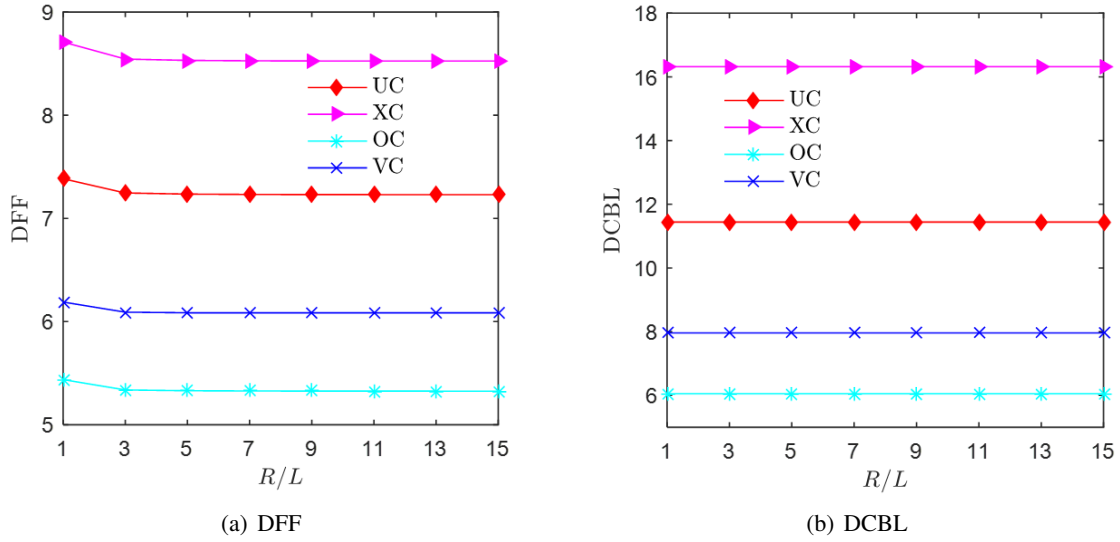
(a) DFF

(b) DCBL

Figure 4. DFF and DCBL of FG-CNTRC curved beams under distribution types with respect to R/L
($L/h = 15$, CF, $V^*_{CNT} = 0.17$)

Additionally, Figs. 3(a) and 3(b) present the DFF and DCBL of the beam ($R/L = 15$, HS, UC) across various volume fractions. The DFF and DCBL are the highest for $V^*_{CNT} = 0.28$ and lowest for $V^*_{CNT} = 0.12$. This indicates that the reinforcement of CNT materials enhances the rigidity of the curved beam.

Consider CF beams with various distribution patterns to investigate the impact of the R/L ratio on DFF and DCBL. Figs. 4(a) and 4(b) illustrate the variation of DFF and DCBL with respect to the R/L ratio. DFF experiences a slight decrease, while DCBL remains relatively unaffected as R/L increases. Furthermore, the DFF and DCBL are the highest for XC beams and smallest for OC ones.

The influence of axial forces on the fundamental frequencies of FG-CNTRC curved beams has been investigated and presented in Tables 7–10 and Figs. 5(a) and 5(b). These results serve as benchmarks for future research. For all boundary conditions, distribution patterns, and volume fractions, the DFF decreases as the tensile axial force in the beam diminishes and the compressive force increases. This phenomenon occurs because a reduction in tensile force or an increase in compressive force results in a decrease in the overall stiffness of the beam. Furthermore, as illustrated in Figs. 5(a) and 5(b), when the compressive force reaches the critical buckling load, the fundamental frequency approaches zero, indicating that the beam becomes instability.

Table 7. Effect of the axial force on DFF of UC curved beams ($L/h = 10, R/L = 5$)

V^*_{CNT}	BC	$\bar{N}_{cr}$	$N_0 = -N_{cr}$ (Tension)	$N_0 = -0.5N_{cr}$ (Tension)	$N_0 = 0$	$N_0 = 0.5N_{cr}$ (Compression)
0.12	HS	18.0497	18.4640	15.9917	13.0583	9.2344
	HH	30.7542	24.4915	21.2535	17.4210	12.4497
	CF	6.9398	7.2531	6.4484	5.4467	4.0307
	CS	23.7900	21.8733	19.0128	15.6100	11.1434
	CH	31.3667	26.2359	23.0408	19.2811	14.4242
	CC	34.7350	28.6709	25.3562	21.4674	16.4712
0.17	HS	28.3150	23.0223	19.9397	16.2822	11.5143

V^*_{CNT}	BC	$\bar{N}_{cr}$	$N_0 = -N_{cr}$ (Tension)	$N_0 = -0.5N_{cr}$ (Tension)	$N_0 = 0$	$N_0 = 0.5N_{cr}$ (Compression)
	HH	47.7661	30.2403	26.2011	21.4107	15.1668
	CF	10.4285	8.9343	7.9391	6.6982	4.9446
	CS	38.3486	27.6685	24.0539	19.7532	14.1052
	CH	50.4188	32.8775	28.8105	24.0099	17.7669
	CC	57.4114	36.3139	32.0291	26.9862	20.4617
0.28	HS	38.9660	26.7669	23.1826	18.9300	13.3866
	HH	63.4088	35.4406	30.9625	25.7111	19.0442
	CF	15.7429	10.6653	9.4857	8.0215	5.9522
	CS	49.9281	31.2489	27.1587	22.2939	15.9104
	CH	65.6089	37.8580	33.3549	28.0787	21.3247
	CC	71.2470	41.0092	36.3765	30.9587	24.0442

Table 8. Effect of the axial force on DFF of XC curved beams ($L/h = 10, R/L = 5$)

V^*_{CNT}	BC	$\bar{N}_{cr}$	$N_0 = -N_{cr}$ (Tension)	$N_0 = -0.5N_{cr}$ (Tension)	$N_0 = 0$	$N_0 = 0.5N_{cr}$ (Compression)
0.12	HS	21.9766	20.3805	17.6519	14.4142	10.1934
	HH	33.7896	25.8283	22.4553	18.4741	13.3439
	CF	9.4731	8.2683	7.3563	6.2290	4.6389
	CS	27.2081	23.3539	20.2933	16.6537	11.8808
	CH	34.6399	27.4754	24.1087	20.1490	15.0517
	CC	37.5719	29.7487	26.2886	22.2283	17.0199
0.17	HS	34.6470	25.4760	22.0654	18.0183	12.7423
	HH	53.9450	32.1583	27.8653	22.7746	16.1418
	CF	14.3222	10.2107	9.0833	7.6857	5.7114
	CS	43.7881	29.4978	25.6336	21.0384	15.0113
	CH	55.6656	34.4258	30.1439	25.0941	18.5547
	CC	61.3446	37.5287	33.0958	27.8833	21.1672
0.28	HS	44.9982	28.7744	24.9216	20.3503	14.3911
	HH	65.7745	36.5275	32.0244	26.7696	20.1710
	CF	20.8753	11.9304	10.6135	8.9951	6.7219
	CS	53.9803	32.4687	28.2125	23.1510	16.5137
	CH	68.3462	38.7079	34.1207	28.7555	21.9313
	CC	73.2088	41.5876	36.8780	31.3684	24.3454

Table 9. Effect of the axial force on DFF of OC curved beams ($L/h = 10, R/L = 5$)

V^*_{CNT}	BC	$\bar{N}_{cr}$	$N_0 = -N_{cr}$ (Tension)	$N_0 = -0.5N_{cr}$ (Tension)	$N_0 = 0$	$N_0 = 0.5N_{cr}$ (Compression)
0.12	HS	11.6117	14.8001	12.8180	10.4664	7.4013
	HH	23.3685	21.5778	18.7927	15.5120	11.3031
	CF	3.8710	5.5822	4.9526	4.1656	3.0575

V^*_{CNT}	BC	$\bar{N}_{cr}$	$N_0 = -N_{cr}$ (Tension)	$N_0 = -0.5N_{cr}$ (Tension)	$N_0 = 0$	$N_0 = 0.5N_{cr}$ (Compression)
	CS	16.9075	18.4818	16.0730	13.2060	9.4363
	CH	23.9384	23.3038	20.5591	17.3363	13.1620
	CC	27.2302	25.6782	22.7965	19.4285	15.1067
0.17	HS	17.9035	18.2947	15.8446	12.9378	9.1489
	HH	37.2400	26.6977	23.1355	18.9106	13.4027
	CF	5.7334	6.8257	6.0504	5.0814	3.7203
	CS	26.9956	23.3055	20.2746	16.6644	11.9116
	CH	38.3600	29.0964	25.5930	21.4589	16.0538
	CC	45.6276	32.5865	28.8074	24.3642	18.5881
0.28	HS	26.5216	22.0662	19.1109	15.6048	11.0349
	HH	52.6837	32.1762	28.0818	23.2722	17.1418
	CF	8.9210	8.3423	7.4028	6.2287	4.5743
	CS	38.3293	27.4356	23.8580	19.6005	14.0043
	CH	54.2116	34.7192	30.6627	25.9071	19.7652
	CC	61.0952	38.1147	33.8788	28.9366	22.6153

Table 10. Effect of the axial force on DFF of VC curved beams ($L/h = 10, R/L = 5$)

| V^*_{CNT}	BC	$\bar{N}_{cr}$	$N_0 = -N_{cr}$ (Tension)	$N_0 = -0.5N_{cr}$ (Tension)	$N_0 = 0$	$N_0 = 0.5N_{cr}$ (Compression)
0.12	HS	14.5046	16.3873	14.1941	11.5914	8.1977
	HH	27.8650	25.3762	22.5610	19.3222	15.3517
	CF	5.0354	6.3145	5.6048	4.7187	3.4698
	CS	20.5206	20.3251	17.6784	14.5259	10.3784
	CH	30.2147	26.4813	23.4370	19.8847	15.3731
	CC	32.6551	27.7667	24.5383	20.7354	15.7987
0.17	HS	22.3357	20.2293	17.5222	14.3093	10.1200
	HH	45.1482	31.6911	28.0658	23.8741	18.6887
	CF	7.4591	7.7148	6.8429	5.7537	4.2213
	CS	32.5563	25.5155	22.1975	18.2437	13.0378
	CH	49.0456	33.1890	29.2757	24.6878	18.8027
	CC	53.6166	35.0175	30.8522	25.9257	19.4709
0.28	HS	31.7377	23.9299	20.7271	16.9261	11.9704
	HH	58.5220	36.8703	32.9145	28.3852	22.8789
	CF	11.4085	9.3084	8.2668	6.9672	5.1333
	CS	43.8127	29.2851	25.4680	20.9225	14.9452
	CH	63.3449	38.3400	34.0530	29.0730	22.8069
	CC	68.0373	39.9990	35.4500	30.1093	23.2269
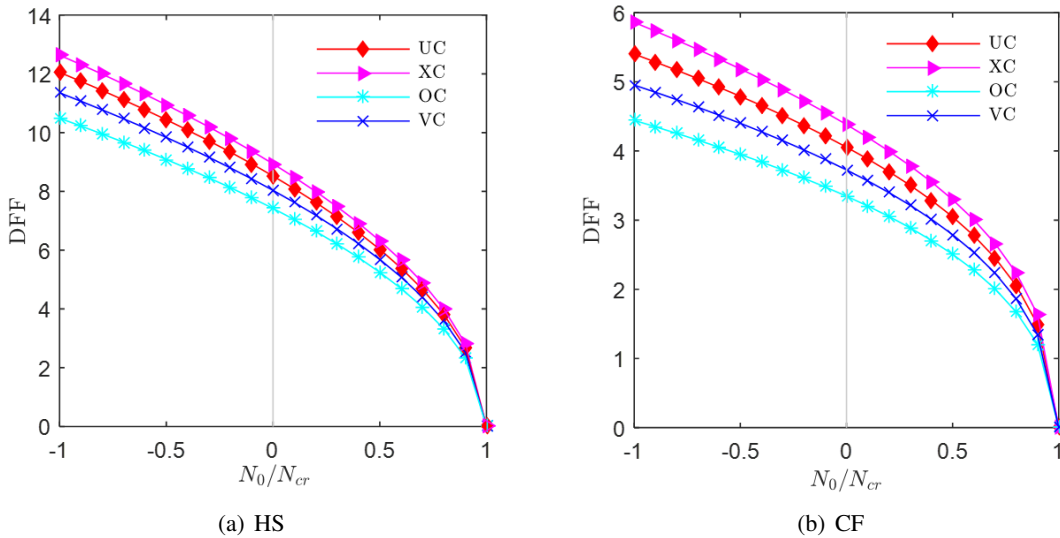
Figure 5. Effect of axial forced on DFF of FG-CNTRC curved beams under various distribution types
($L/h = 5, R/L = 5, V^*_{CNT} = 0.12$)

4. Conclusions

This study employs the Ritz method and higher-order shear deformation theory to analyze the free vibration of axially loaded FG-CNTRC curved beams. The governing equations are derived based on the Lagrange's equation. Numerical examples are conducted to validate the findings and investigate the influence of boundary condition, slenderness, curvature, CNT distribution, and volume fraction on the beams' frequency and critical buckling loads. The results demonstrate that the methodologies and theoretical framework presented in this research are both straightforward and effective for analyzing the free vibration of axially loaded FG-CNTRC curved beams.

Acknowledgment

References

[1] Duc, N. D., Lee, J., Nguyen-Thoi, T., Thang, P. T. (2017). Static response and free vibration of functionally graded carbon nanotube-reinforced composite rectangular plates resting on Winkler–Pasternak elastic foundations. *Aerospace Science and Technology*, 68:391–402.

[2] Nguyen, T. N., Thai, C. H., Nguyen-Xuan, H., Lee, J. (2018). NURBS-based analyses of functionally graded carbon nanotube-reinforced composite shells. *Composite Structures*, 203:349–360.

[3] Hai, L. V., Lieu, Q. X. (2024). Dynamic analysis of carbon nanotube-reinforced composite plates using reduced order isogeometric model. *Journal of Science and Technology in Civil Engineering (JSTCE) - HUCE*, 18(4):69–82.

[4] Hajianmaleki, M., Qatu, M. S. (2013). Vibrations of straight and curved composite beams: A review. *Composite Structures*, 100:218–232.

[5] Wattanasakulpong, N., Ungbhakorn, V. (2013). Analytical solutions for bending, buckling and vibration responses of carbon nanotube-reinforced composite beams resting on elastic foundation. *Computational Materials Science*, 71:201–208.

[6] Pham, S. D., Karamanli, A., Wattanasakulpong, N., Vo, T. P. (2024). A Quasi-3D theory for bending, vibration and buckling analysis of FG-CNTRC and GPLRC curved beams. *Structures*, 63:106431.

[7] Shi, Z., Yao, X., Pang, F., Wang, Q. (2017). A semi-analytical solution for in-plane free vibration analysis of functionally graded carbon nanotube reinforced composite circular arches with elastic restraints. *Composite Structures*, 182:420–434.

[8] Allahkarami, F., Nikkhah-bahrami, M., Saryazdi, M. G. (2018). Magneto-thermo-mechanical dynamic buckling analysis of a FG-CNTs-reinforced curved microbeam with different boundary conditions using strain gradient theory. *International Journal of Mechanics and Materials in Design*, 14(2):243–261.

[9] Zhang, Y., Zhang, B., Shen, H., Wang, Y., Zhang, X., Liu, J. (2020). Nonlinear Bending Analysis of Functionally Graded CNT-Reinforced Shallow Arches Placed on Elastic Foundations. *Acta Mechanica Solida Sinica*, 33(2):164–186.

[10] Babaei, H. (2022). Free vibration and snap-through instability of FG-CNTRC shallow arches supported on nonlinear elastic foundation. *Applied Mathematics and Computation*, 413:126606.

[11] Lezgy-Nazargah, M., Karamanli, A., Vo, T. P. (2023). Bending, buckling and free vibration analyses of shallow-to-deep FG curved sandwich beams using a global–local refined shear deformation theory. *Structures*, 52:568–581.

[12] Phung-Van, P., Hung, P. T., Tangaramvong, S., Nguyen-Xuan, H., Thai, C. H. (2025). A novel Chebyshev-based both meshfree method and shear deformation theory for functionally graded triply periodic minimal surface flat plates. *Computers & Structures*, 309:107660.

[13] Hosseini, S. A. H., Rahmani, O. (2016). Free vibration of shallow and deep curved FG nanobeam via nonlocal Timoshenko curved beam model. *Applied Physics A*, 122(3):169.

[14] Pei, Y. L., Li, L. X. (2021). A simplified theory of FG curved beams. *European Journal of Mechanics - A/Solids*, 85:104126.

[15] Trien, T. T., Phong, L. T., Hung, P. T. (2025). Isogeometric free vibration of the porous metal foam plates resting on an elastic foundation using a quasi-3D refined theory. *Journal of Science and Technology in Civil Engineering (JSTCE) - HUCE*, 19(1):119–130.

[16] Sayyad, A. S., Ghugal, Y. M. (2019). A sinusoidal beam theory for functionally graded sandwich curved beams. *Composite Structures*, 226:111246.

[17] Hong, N. T. (2025). A novel isogeometric model for free vibration, buckling, and transient response of double-layer BFGP curved beams with elastic boundary condition using modified first-order shear theory. *Mechanics Based Design of Structures and Machines*, 53(7):5119–5151.

[18] Nhan, N. T., Duong, N. N., Kien, N. T. (2024). Free vibration analysis of laminated composite shallow curved beam with various boundary conditions. *Journal of Science and Technology in Civil Engineering (JSTCE) - HUCE*, 18(3):1–18.

[19] Ke, L.-L., Yang, J., Kitipornchai, S. (2010). Nonlinear free vibration of functionally graded carbon nanotube-reinforced composite beams. *Composite Structures*, 92(3):676–683.

[20] Yas, M. H., Samadi, N. (2012). Free vibrations and buckling analysis of carbon nanotube-reinforced composite Timoshenko beams on elastic foundation. *International Journal of Pressure Vessels and Piping*, 98:119–128.

[21] Karamanli, A., Wattanasakulpong, N., Lezgy-Nazargah, M., Vo, T. P. (2023). Bending, buckling and free vibration behaviours of 2D functionally graded curved beams. *Structures*, 55:778–798.

[22] Huynh, T.-A., Luu, A.-T., Lee, J. (2017). Bending, buckling and free vibration analyses of functionally graded curved beams with variable curvatures using isogeometric approach. *Meccanica*, 52(11–12): 2527–2546.

[23] Alhajahmad, A., Mittelstedt, C. (2025). Ritz-Legendre approach for capturing the mode jumping phenomena in variable-stiffness composite fuselage panels. *Composite Structures*, 357:118946.

Appendix [6]

$$K_{ij}^{11} = \left(A + \frac{2B}{R} + \frac{C}{R^2} - \frac{2D}{R} - \frac{2E}{R^2} + \frac{F}{R^2}\right) \int_0^L \psi_{i,x}\psi_{j,x}dx + \frac{G}{R^2} \int_0^L \psi_i\psi_j dx \tag{A.1}$$

$$K_{ij}^{12} = \left(D - \frac{C}{R} - B - \frac{F}{R} + \frac{2E}{R}\right) \int_0^L \psi_{i,x}\varphi_{j,xx}dx - \frac{G}{R} \int_0^L \psi_i\varphi_{j,x}dx + \left(\frac{A}{R} + \frac{B}{R^2} - \frac{D}{R^2}\right) \int_0^L \psi_{i,x}\varphi_j dx \tag{A.2}$$

$$K_{ij}^{13} = \left(D + \frac{E}{R} - \frac{F}{R}\right) \int_0^L \psi_{i,x}\xi_{j,x}dx - \frac{G}{R} \int_0^L \psi_i\xi_j dx \tag{A.3}$$

$$K_{ij}^{22} = \frac{A}{R^2} \int_0^L \varphi_i\varphi_j dx + (C + F - 2E) \int_0^L \varphi_{i,xx}\varphi_{j,xx}dx + G \int_0^L \varphi_{i,x}\varphi_{j,x}dx$$
$$+ \left(\frac{D}{R} - \frac{B}{R}\right)\left(\int_0^L \varphi_{i,xx}\varphi_j dx + \int_0^L \varphi_i\varphi_{j,xx}dx\right) \tag{A.4}$$

$$K_{ij}^{23} = (F - E) \int_0^L \xi_{i,x}\varphi_{j,xx}dx + G \int_0^L \xi_i\varphi_{j,x}dx + \frac{D}{R} \int_0^L \xi_{i,x}\varphi_j dx \tag{A.5}$$

$$K_{ij}^{33} = G \int_0^L \xi_i\xi_j dx + F \int_0^L \xi_{i,x}\xi_{j,x}dx \tag{A.6}$$

$$M_{ij}^{11} = \left(H + \frac{2I}{R} + \frac{J}{R^2} - \frac{2K}{R} - \frac{2M}{R^2} + \frac{N}{R^2}\right) \int_0^L \psi_i\psi_j dx \tag{A.7}$$

$$M_{ij}^{12} = \left(K - I - \frac{J}{R} + \frac{2M}{R} - \frac{N}{R}\right) \int_0^L \psi_i\varphi_{j,x}dx \tag{A.8}$$

$$M_{ij}^{13} = \left(K + \frac{M}{R} - \frac{N}{R}\right) \int_0^L \psi_i\xi_j dx \tag{A.9}$$

$$M_{ij}^{22} = H \int_0^L \varphi_i\varphi_j dx + (J - 2M + N) \int_0^L \varphi_{i,x}\varphi_{j,x}dx \tag{A.10}$$

$$M_{ij}^{23} = (N - M) \int_0^L \xi_i\varphi_{j,x}dx \tag{A.11}$$

$$M_{ij}^{33} = N \int_0^L \xi_i\xi_j dx \tag{A.12}$$

$$K_{Gij}^{11} = \frac{1}{R^2} \int_0^L \psi_i \psi_j dx \tag{A.13}$$

$$K_{Gij}^{12} = -\frac{1}{R} \int_0^L \psi_i \varphi_{j,x} dx \tag{A.14}$$

$$K_{Gij}^{22} = \int_0^L \varphi_{i,x} \varphi_{j,x} dx \tag{A.15}$$

$$\mathbf{d} = \begin{bmatrix} u_{0j} & w_{0j} & \theta_{0j} \end{bmatrix}^T \tag{A.16}$$